Feasibility assessment of non-contact acoustic emission monitoring of corrosion-fatigue damage in submerged steel structures

Riccioli, Filippo; Alkhateeb, Sarjoon; Mol, Arjan; Pahlavan, Lotfollah

DOI
10.1016/j.oceaneng.2024.119296

Publication date
2024

Document Version
Final published version

Published in
Ocean Engineering

Citation (APA)
Riccioli, F., Alkhateeb, S., Mol, A., & Pahlavan, L. (2024). Feasibility assessment of non-contact acoustic emission monitoring of corrosion-fatigue damage in submerged steel structures. *Ocean Engineering*, *312*, Article 119296. https://doi.org/10.1016/j.oceaneng.2024.119296

Ocean Engineering 312 (2024) 119296

Contents lists available at ScienceDirect

Ocean Engineering

journal homepage: www.elsevier.com/locate/oceaneng

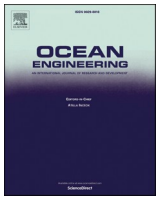

Research paper

Feasibility assessment of non-contact acoustic emission monitoring of corrosion-fatigue damage in submerged steel structures

Filippo Riccioli [a,*], Sarjoon Alkhateeb [a], Arjan Mol [b], Lotfollah Pahlavan [a]

[a] Department of Maritime and Transport Technology, Delft University of Technology, 2628CD, Delft, the Netherlands
[b] Department of Materials Science and Engineering, Delft University of Technology, 2628CD, Delft, the Netherlands

ARTICLE INFO

Keywords:
Acoustic emission
Corrosion-fatigue
Damage detection
Damage monitoring
Offshore support structures

ABSTRACT

Corrosion-fatigue is considered to be one of the main degradation mechanisms affecting the structural integrity of offshore support structures. This paper presents a feasibility assessment for the detection and monitoring of corrosion-fatigue damage using non-contact acoustic emission (AE). An accelerated corrosion-fatigue experiment was conducted on a S420NL dog-bone specimen. A corrosion-fatigue cell was designed and fabricated to simultaneously apply accelerated corrosion and cyclic loads on the specimen submerged in artificial seawater. A three-electrode electrochemical configuration under potentiostatic control was used to accelerate corrosion. The ultrasound signals were continuously measured using underwater AE transducers (in the frequency range of 50–450 kHz) placed at a fixed distance from the tested coupon. The results of the accelerated corrosion-fatigue experiment suggest that corrosion-fatigue-induced ultrasound signals can be detected with a satisfactory signal-to-noise ratio using non-contact AE sensors. The mean energy of the corrosion-fatigue-induced ultrasound signals was one order of magnitude higher than that of the corrosion-induced signals. The trends of the AE parameters extracted from the AE signals were analysed as functions of the load cycles. The results revealed high potential for the identification and monitoring of corrosion-fatigue damage using the non-contact AE technique.

1. Introduction

Offshore support structures and mooring systems are key assets for energy production at sea, supporting installations such as wind turbines, photovoltaic islands, and floating production-storage-offloading units (FPSOs). Corrosion, fatigue, and their simultaneous combination (i.e. corrosion-fatigue) are considered to be the prevalent failure modes of offshore support structures (Adedipe et al., 2016; Arzaghi et al., 2018; Du et al., 2020; Fontaine et al., 2014a, 2014b; Lone et al., 2022a, 2022b; Ma et al., 2013; Melchers et al., 2012). A detailed assessment of the structural integrity of the submerged parts of these structures can be challenging because of their difficult-to-access locations, waves, weather conditions, and marine growth.

Visual inspection can provide a fast and general overview of the structural integrity and possibly allow the determination of the location of damage (after cleaning of the surface). However, this technique can detect only large surface defects. The results of the analysis can be affected by the clarity of seawater, and it often requires further local damage inspection using more advanced NDT methods after surface cleaning (Assaker, 2020).

Magnetic particle inspection (MPI) is commonly used to detect surface and near-surface flaws in ferromagnetic materials (Rizzo, 2013). MPI has been successfully applied for underwater inspection and/or monitoring (Caines et al., 2013; Forsyth, 2011; Bhandari et al., 2015). The results of MPI, such as the true length of discontinuities, can be obtained faster than by other NDT methods (Zawawi et al., 2019). However, deeply embedded flaws cannot be detected using this technique, and it requires surface cleaning (Assaker, 2020).

Ultrasonic testing is suitable for the detection of subsurface defects and thickness measurements (Rizzo, 2013) and allows the location and estimation of the size of corrosion-fatigue cracks (Caines et al., 2013). However, without proper surface preparation, the influence of surface roughness (often with many small pits) on the test results reduces the accuracy and reliability of the method. Guided ultrasonic waves (GUWs) can also be used to locate cracks and notches by probing larger structural areas at a few monitoring points. However, this approach requires proper coupling between the material surface (after preparation and cleaning) and probes and is also adversely affected by structural joints and discontinuities.

Radiography techniques are effective for imaging the internal

* Corresponding author. Delft University of Technology, Mekelweg 2, 2628CD, Delft, the Netherlands.
E-mail address: f.riccioli@tudelft.nl (F. Riccioli).

https://doi.org/10.1016/j.oceaneng.2024.119296
Received 7 February 2024; Received in revised form 14 August 2024; Accepted 16 September 2024
Available online 20 September 2024

structure of an assessed structure using high-energy electromagnetic waves that penetrate the material and can be used to detect internal and surface defects with minimal surface preparation (Zawawi et al., 2019). In this context, its use can be limited because of safety hazards and the limited accessibility of the submerged structures under inspection (typically, the test material must be accessible from both sides) (Rizzo, 2013). Studies have shown observations of corrosion-fatigue crack growth using in-situ 3D x-ray tomography in laboratory environment (Qian et al., 2024; Stannard et al., 2018).

Eddy-current (EC) testing allows for the quick detection of surface and near-surface defects with minimal surface preparation (being a non-contact technique). However, the results of EC measurements can be affected by the material surface condition, and experienced operators and specialised tools are typically required (Zawawi et al., 2019). Alternating current field measurement (ACFM) is a non-contact electromagnetic technique used to detect and measure surface-breaking cracks (Rizzo, 2013). This technique can be used for damage detection with coatings of varying thicknesses; however, it is only applicable to surface defects.

Given the electrochemical nature of the corrosion process, electrochemical techniques have gained widespread application in the assessment and monitoring of corrosion-fatigue (Roberge, 2008). Electrochemical impedance spectroscopy (EIS) has been extensively investigated for corrosion monitoring (Kim et al., 2019; Mansfeld and Little, 1991; McCluney et al., 1992; Ribeiro and Abrantes, 2016; Wang et al., 2014, 2020; Zhang and Hoogeland, 2019; Zhang et al., 2022). To retrieve the state of degradation of protective coatings and the corrosion rate of the underlying metals in the monitored area, EIS must be interpreted with the help of complex and ambiguous equivalent electrical circuit modelling by highly qualified experts. Furthermore, in situations where samples from the material are to be taken, EIS cannot be considered a non-invasive technique.

Acoustic emission (AE) is a passive ultrasound method that is widely recognised as an effective monitoring technique for assessing corrosion, fatigue, and corrosion-fatigue damage (Alkhateeb et al., 2022; Calabrese and Proverbio, 2020; Huijer et al., 2021; Pahlavan et al., 2014; Scheeren et al., 2022, 2023; Van Steen et al., 2019). The AE technique allows the identification, localisation, and characterisation of damage by monitoring transient stress waves (i.e. acoustic emission events) generated by the rapid release of energy from localised sources within the material (Grosse, 2008). Every relevant AE event can be linked to the onset of new damage or the progression of an active defect in the material structure. Each possible AE source during the evolution of corrosion-fatigue damage can be described by its specific properties, such as amplitude, count, and energy (Yuyama et al., 1984). Various approaches have been proposed for characterising and monitoring AE activity during damage evolution (Aggelis et al., 2011; Bi et al., 2020; Calabrese et al., 2015; Calabrese and Proverbio, 2020; Chai et al., 2017; Chai et al., 2022a; Chai et al., 2022b; Chang et al., 2005; Chang et al., 2005; Chang et al., 2005; Du et al., 2011; Fregonese et al., 2001; Han et al., 2011; Hwang et al., 2015; Jirarumgsatian and Prateepasen, 2010; Li et al., 2015; Skal'sʼ Kyi et al., 2017). The primary mechanisms responsible for the generation of AE are pitting, crack initiation, and/or propagation (Chai et al., 2017; Fregonese et al., 2001; Jirarumgsatian and Prateepasen, 2010; Yuyama et al., 1984). Secondary mechanisms can also be present in the context of corrosion monitoring, such as hydrogen bubble evolution (and friction at crack walls), debris fracturing, and corrosion product formation on metal surfaces (Ferrer et al., 2002; Jirarumgsatian and Prateepasen, 2010; Yuyama et al., 1984). Recently, the authors investigated the detectability of AE signals during underwater corrosion using non-contact transducers (Alkhateeb et al., 2022).

Existing methods for assessing the integrity of submerged steel structures are generally limited to surface defects and require surface preparation, that is, cleaning. Imprecise coupling between the material surface and probes further compromises the accuracy of the test results. Safety concerns, limited accessibility of the structure under assessment, and the need for qualified operators and experts restrict their applicability. Among these methods, AE offers high potential for monitoring and characterising corrosion-fatigue damage in submerged steel structures.

Conventional approaches emphasize the necessity of contact between AE transducers and the material surface (Calabrese and Proverbio, 2020; Grosse, 2008). This can facilitate the realization of high signal-to-noise ratio and precise AE source localisation. However, in scenarios involving complex geometries or inaccessible areas (e.g. submerged offshore structures), achieving proper coupling between the sensors and the material surface may be challenging. Non-contact AE offers a non-intrusive solution for measurements in such environments. Nonetheless, this technique may offer a lower signal-to-noise ratio and increased susceptibility to external disturbances (e.g. ambient noise). Assessing the detectability of AE signals, considering factors such as signal-to-noise ratio, AE energy, and number of AE signals measured during corrosion-fatigue, is crucial for enabling a non-intrusive integrity assessment of submerged offshore structures and mooring systems. The use of the underwater AE technique in a non-contact manner to measure corrosion-fatigue-induced ultrasound signals has not been reported to the authors' knowledge, and it represents the distinct contribution and novelty of this work.

This study aims to demonstrate the feasibility of detecting and monitoring corrosion-fatigue damage in submerged steel structures using non-contact AE measurements. The findings of this study are expected to pave the way for more efficient and environmentally friendly procedures for integrity assessment of mooring systems, while enhancing the safety of energy production offshore. Corrosion-fatigue experiments were conducted on a dog-bone steel specimen. The AE parameters extracted from the measured signals were analysed as a function of the load cycles to assess the detectability and evolution of corrosion-fatigue-induced ultrasound signals.

2. Non-contact acoustic emission (AE) monitoring of corrosion-fatigue damage

Fig. 1 shows a schematic illustration of the non-contact AE measurement for a steel specimen submerged in seawater and subjected to corrosion-fatigue degradation.

Damage-induced ultrasound waves can propagate in steel media as bulk waves (following longitudinal and shear mode), surface (i.e. Rayleigh) waves, or guided waves, depending on the frequency of the waves and the thickness of the medium (Grosse, 2008; Pahlavan et al., 2014). When reaching and propagating through seawater, ultrasound waves propagate (at a constant speed) as pressure waves. Reflected and transmitted waves are generated at the interface between the two media (Krautkrämer and Krautkrämer, 2013). The attenuation (of the transmitted) and reflection of ultrasound waves depend on the characteristic acoustic impedance r and speed of sound c in the two media (and the incident angle) (Kinsler et al., 2000). Ultrasound wave components with sufficient energy (to overcome geometrical spreading and material attenuation) can reach the transducer. In the present study, for the corrosion-fatigue damage type of interest, it is feasible to assume that the source signal S is generated by surface defects (Fig. 1). In the frequency domain, the measured signal P can be described as the convolution of the source signal S with the propagation (transfer) function of water, W_w, and the transducer transfer function, D, as follows:

$$P = DW_wS + N \tag{1}$$

where N refers to the background noise and neglected components of the ultrasound wave, for example reflections from neighbouring surfaces. When N is sufficiently small, the measured damage-induced set of signals may be described as

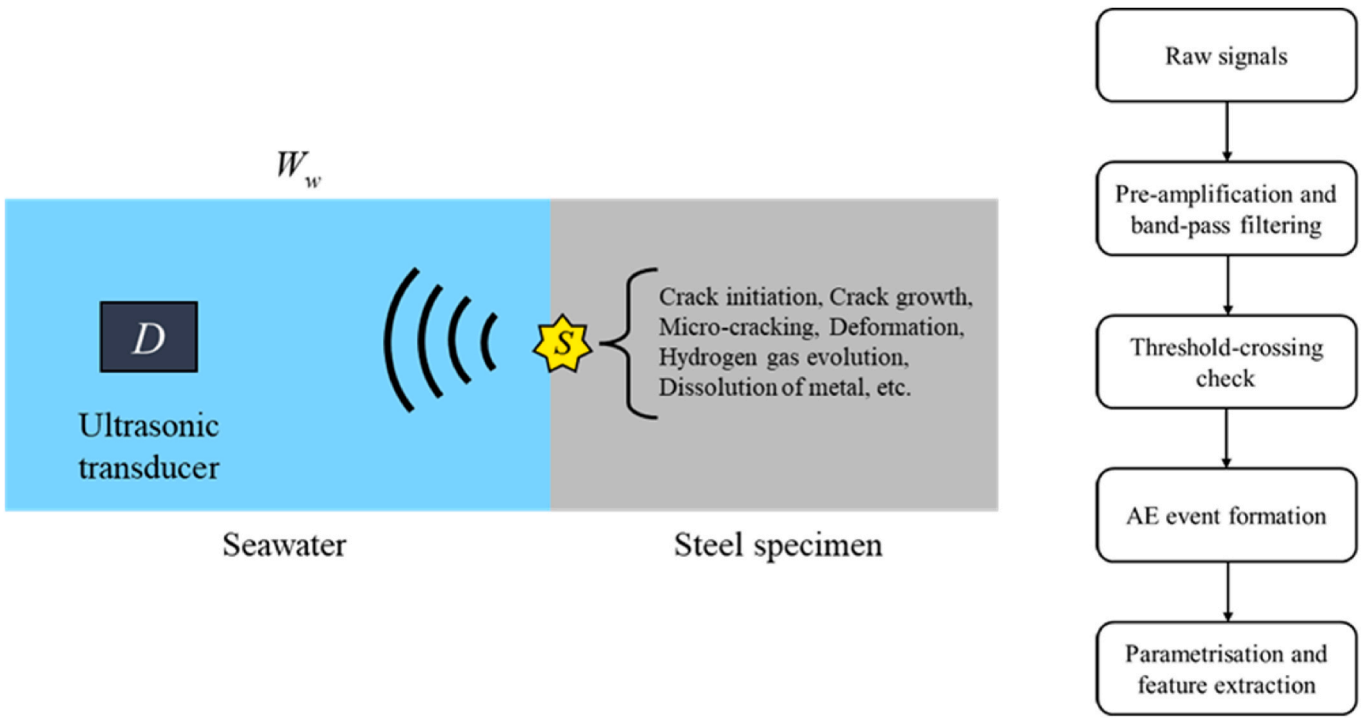

Fig. 1. Schematic illustration of underwater non-contact AE measurement (left) and signal analysis process (right).

$$\sum_i P_i = \sum_i D W_w S_{n_i} \tag{2}$$

where n is an indicator equal to 1 in the case of a corrosion-induced source ($S_{corrosion\text{-}induced}$), and 2 in the case of a corrosion-fatigue-induced source ($S_{corrosion\text{-}fatigue\text{-}induced}$). If the two source mechanisms are separated, their respective total released energy can be approximated as

$$\begin{aligned} E_{n_{total}} &= \sum_i E_{n_i} = \sum_i \int (P_{n_i})^2 d\omega = \sum_i \int (D W_w S_{n_i})^2 d\omega \\ &= \sum_i \int (Z S_{n_i})^2 d\omega = \sum_i \sum_j \Delta\omega Z_j^2 S_{n_{ij}}^2 \end{aligned} \tag{3}$$

where Z denotes the consolidation of propagation transfer functions on the path from the source S to the ultrasonic receiver (Scheeren et al., 2023).

2.1. AE sources during corrosion-fatigue

Acoustic emissions during the evolution of corrosion-fatigue damage can be generated by several mechanisms. Typically, resonance-type piezoelectric transducers are used for measuring these signals. For each damage mechanism, the AE source can be described by its specific properties, such as amplitude, count, and energy (Chai et al., 2022a; Chang et al., 2005). Dissolution of metal or breakdown of thin passive film are typically characterised by the lowest AE energy level (proportional to peak amplitude, typically less than 10 μV) (Jirarungsatian and Prateepasen, 2010; Meyer et al., 2013). These AE events are considered detectable only by highly sensitive measurement systems. The fracture of thick oxide films is associated with AE with relatively small amplitudes (in the order of 10 μV) (Meyer et al., 2013). Hydrogen bubble evolution due to hydrogen ion reduction in acid solutions can generate ultrasound signals characterised by higher energy levels and peak amplitudes at approximately 0.1–1 mV (Meyer et al., 2013; Nuthalapati et al., 2023). A similar energy level characterises slip or twin deformation (in which continuous-type AE are typically observed) (Nuthalapati et al., 2023). Microcracking mechanisms (e.g. cleavage and/or intergranular cracking and separations) can provide an AE energy level of intermediate magnitude with a peak amplitude on the order of 1–10 mV (Calabrese and Proverbio, 2020; Nuthalapati et al., 2023). The highest AE energy level (above 10 mV) is expected from macrocracking, as a result of the large-scale cleavage or coalescence of microcracks (Calabrese and Proverbio, 2020; Meyer et al., 2013; Nuthalapati et al., 2023). Furthermore, specific AE sources can be related to the fracture or decohesion of precipitates, second-phase particles, and/or non-metallic inclusions in the crack tip plastic zone (Meyer et al., 2013; Du et al., 2011).

2.2. Detection and identification of corrosion-fatigue damage using non-contact AE

The parametrization of the AE signals was considered in this investigation to extract their main features, as graphically shown in Fig. 2. The peak amplitude, energy, and counts were analysed for all the sensors used to investigate the feasibility of detecting and monitoring corrosion-fatigue-induced signals using non-contact AE measurements.

In this study, variations in peak amplitude, energy, and counts were analysed as a function of load cycles to assess the detectability of corrosion-fatigue-induced ultrasound signals using non-contact AE transducers.

The variation and evolution of the hit rates and cumulative AE parameters (e.g. number of burst-type signals, energy, and counts) were calculated as functions of the load cycles to assess the evolution of the corrosion-fatigue damage. By evaluating the cumulative trends of AE parameters as a function of time (and/or load cycles), different stages of damage growth can be defined (Calabrese et al., 2015; Chai et al., 2017, 2022b; Han et al., 2011; Li et al., 2015).

The variation of AE burst hit rate (i.e. rate of burst-type signals per load cycles and/or time unit), energy rate, and count rate throughout the duration of the corrosion-fatigue experiment were analysed to monitor active AE sources and provide insights into the various stages of damage growth. Considering the nature of AE signals, every relevant AE event can indicate the onset of new damage, the progression of an active

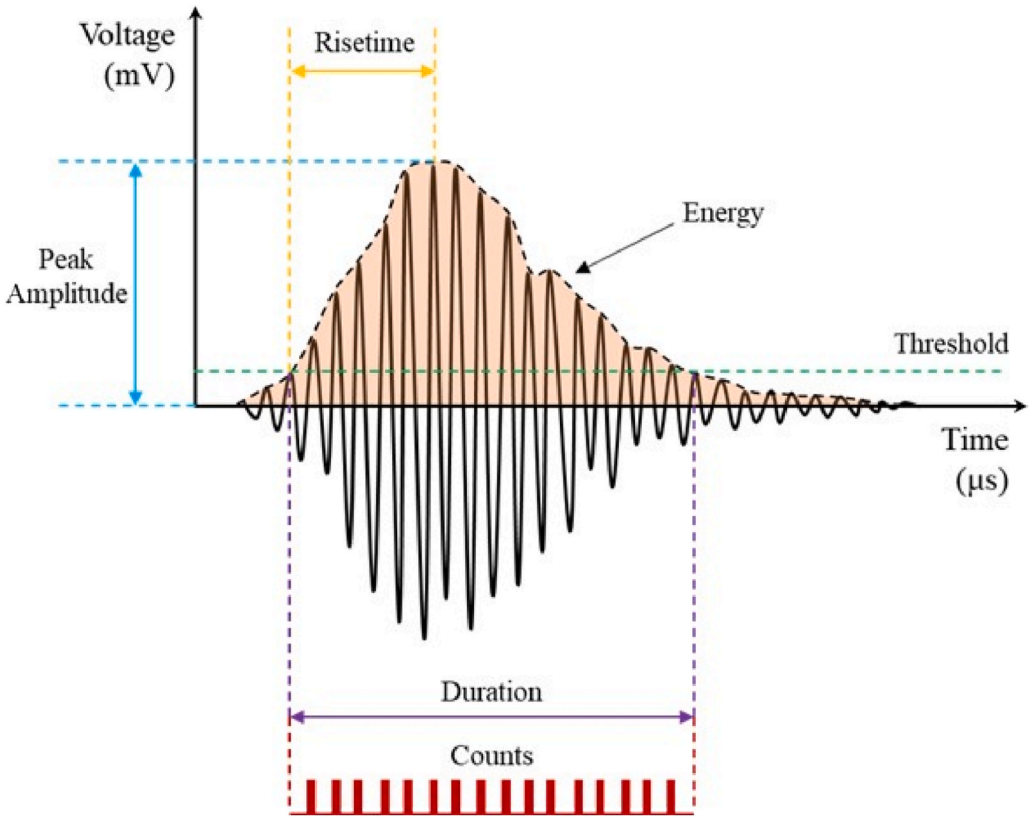

Fig. 2. Schematic illustration of the AE signal waveform and parameters. *Peak amplitude* is the value of the highest peak of the measured signal (in Voltage), typically expressed in decibels (dB). *Energy* (in eu, and/or V^2s) represents the area measured under the envelope of the recorded signal waveform. *Counts* (an absolute number) is the number of signal amplitude peaks greater than the threshold value.

defect, and/or the occurrence of plastic deformations in the material structure. The AE burst hit rate can provide information on the damage growth rate.

The coefficients of variance (CV) of the peak amplitude, energy, and counts were calculated and compared to quantify the parameter performance for the detection and identification of damage. The mean energies of the AE signals were calculated for each stage of damage growth. Analysis of the mean energy can provide valuable insights into the energy characteristics of corrosion- and corrosion-fatigue-induced signals at different stages of damage evolution.

3. Material and methods

Accelerated corrosion-fatigue experiments were conducted on a dog-bone steel specimen to assess the detectability of damage-induced ultrasound signals using non-contact AE transducers. In the context of this feasibility investigation, corrosion and fatigue were simultaneously accelerated at different rates.

3.1. Experimental setup and test specimen

A dedicated experimental setup was designed and fabricated to simultaneously apply accelerated corrosion and cyclic loads on a dog-bone steel specimen submerged in artificial seawater. Fig. 3 shows a schematic of the corrosion-fatigue test setup and instrumentation.

Fig. 4 (left) shows the corrosion-fatigue cell. An aluminium support frame (Fig. 5a) was fabricated to accommodate the 630x630 × 630mm^3 Plexiglas tank between the two grips of the mechanical testing machine.

A circular hole was created at the centre of the bottom of the tank (Fig. 5b) with a dedicated sealing mechanism around the connector disk. A cutout was realised in the centre of the connector disk with the same dimensions as the shoulder of the steel specimen for installation. The connector disk was bolted to the bottom of the tank using six bolted connections (Fig. 5c). Sealed coupling between the specimen and the disk was achieved using a thick layer of elastic glue. The design (Fig. 5d) ensured a watertight connection between the steel specimen submerged in artificial seawater and the lower clamp of the fatigue testing machine.

Fig. 6 shows a schematic of the dog-bone steel specimen. The chosen material for the dog-bone specimen, that is, S420NL, was characterised by a yield stress of 420 N/mm^2, a tensile strength of 480–620 N/mm^2, and an elongation of 20%. The mechanical properties of the selected material were in the range of those characteristic of the R3 steel grade (a typical steel grade for offshore support structures, e.g. mooring chains). The specimen was designed according to ASTM E8/E8M standards (ASTM E8/E8M-22, 2022). Since the damage-induced signals immediately enter the seawater and propagate towards the sensors in a non-dispersive manner (geometric spreading is the leading factor influencing signal amplitude attenuation in the considered frequency range), the geometry of the test sample is expected to have no notable influence on the conclusions. The general trends of the AE measurements could hold for other underwater steel structures. However, further investigation will be needed to extend the findings of this study.

The dog-bone steel specimen was prepared before the test to induce corrosion-fatigue damage in a constrained area of the steel specimen. This area is a half-circle (2 cm of diameter) exposed surface located at the edge of the width of the specimen, in line with the centre of the gauge area (and extended in the width and thickness directions), as shown in Fig. 4 (right) and 6.

3.2. Accelerated corrosion-fatigue process

A three-electrode electrochemical configuration under potentiostatic control was used to accelerate corrosion. The exposed surface of the dog-bone working electrode steel specimen and a graphene bar as counter

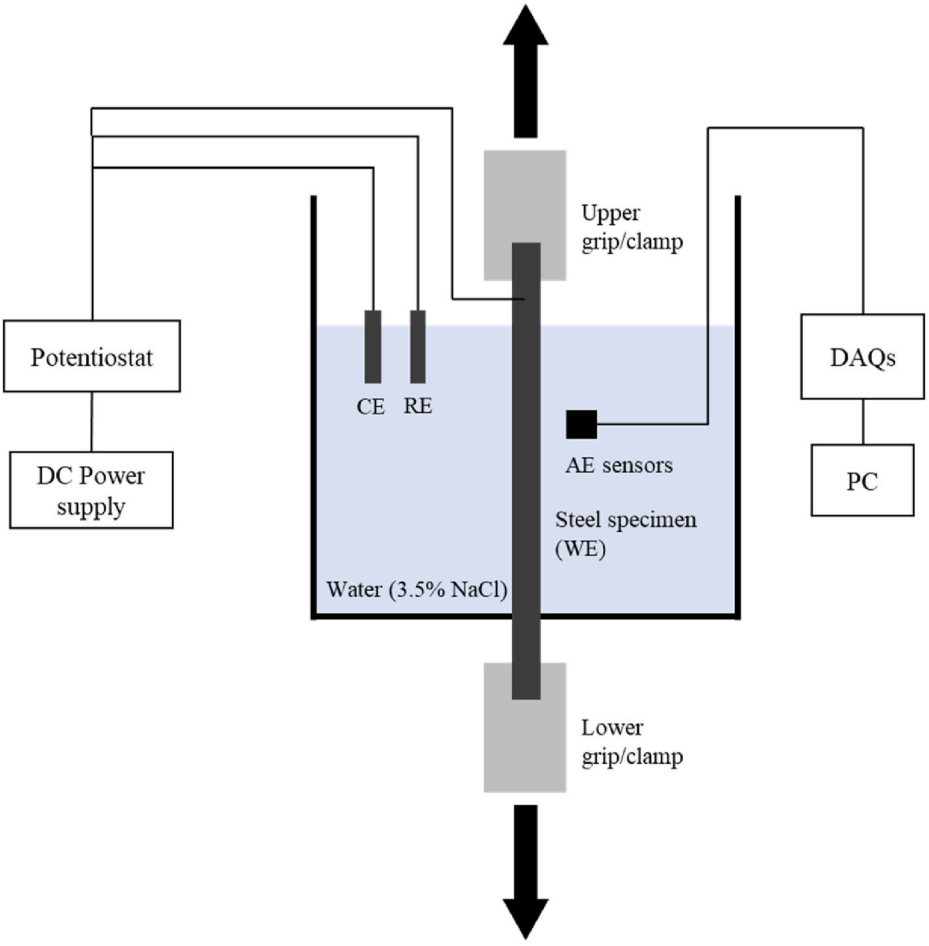

Fig. 3. Schematic illustration of the corrosion-fatigue test setup and instrumentation.

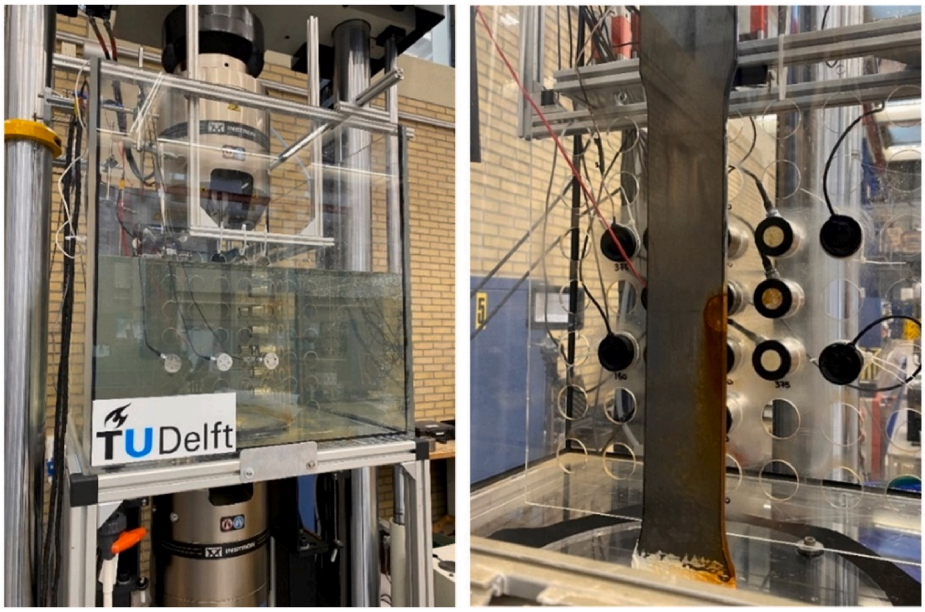

Fig. 4. The corrosion-fatigue cell located between the two grips of a bi-axial Instron fatigue testing machine (left) and pre-corroded steel specimen (right).

electrode were submerged in artificial seawater, i.e. a 3.5 wt-% sodium chloride aqueous solution. A reference silver/silver chloride electrode (Ag/AgCl) with a stable and well-known potential completed the three-electrode system, allowing the potentiostatic control of the steel specimen with respect to the reference electrode. A fixed potential, equal to $-0.435\ V_{Ag/AgCl}$, was imposed allowing to measure the current between

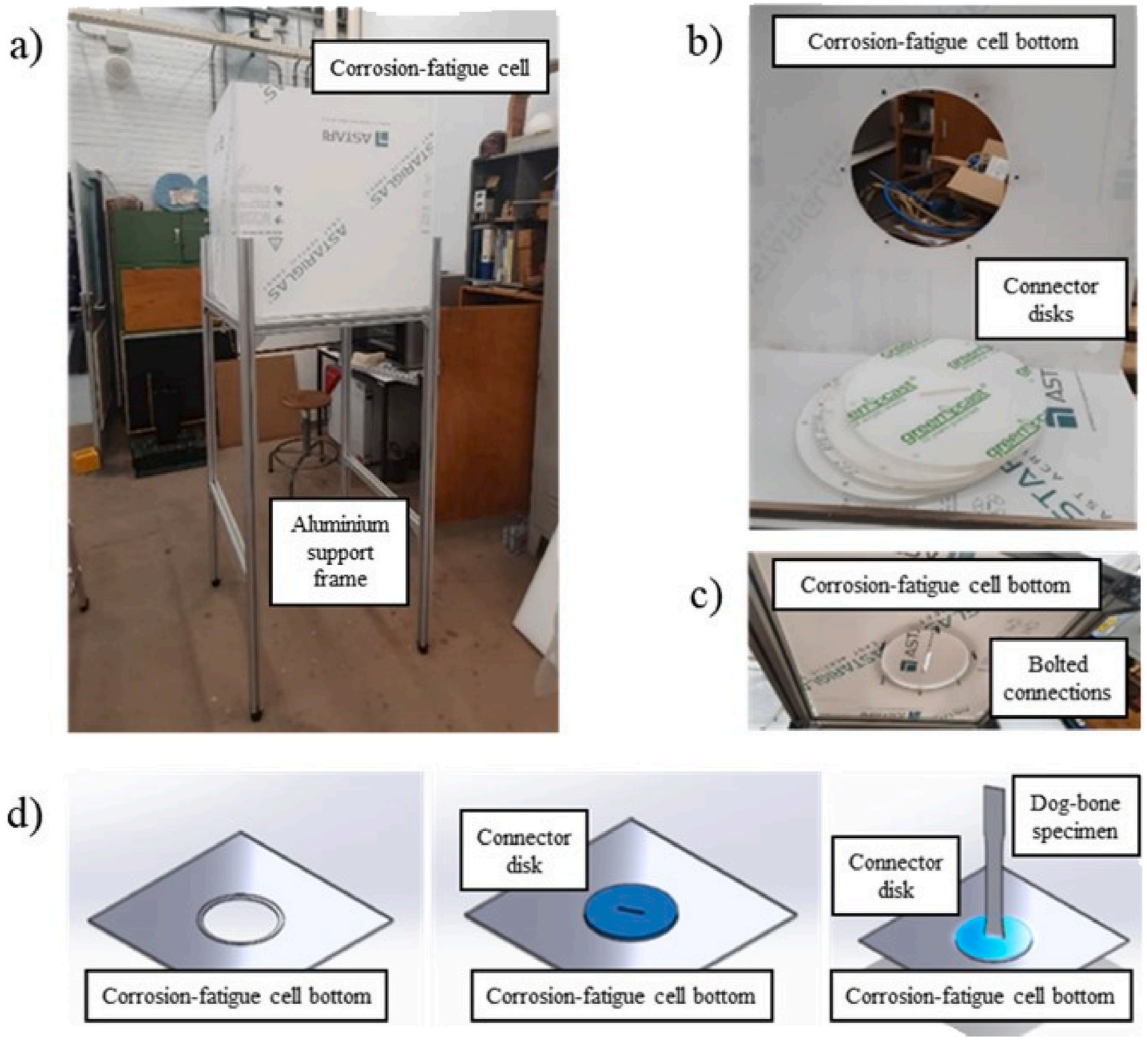

Fig. 5. (a) Preparation of the corrosion-fatigue cell and aluminium support frame; (b–c) preparation of sealing mechanism; (d) schematic of the seal design.

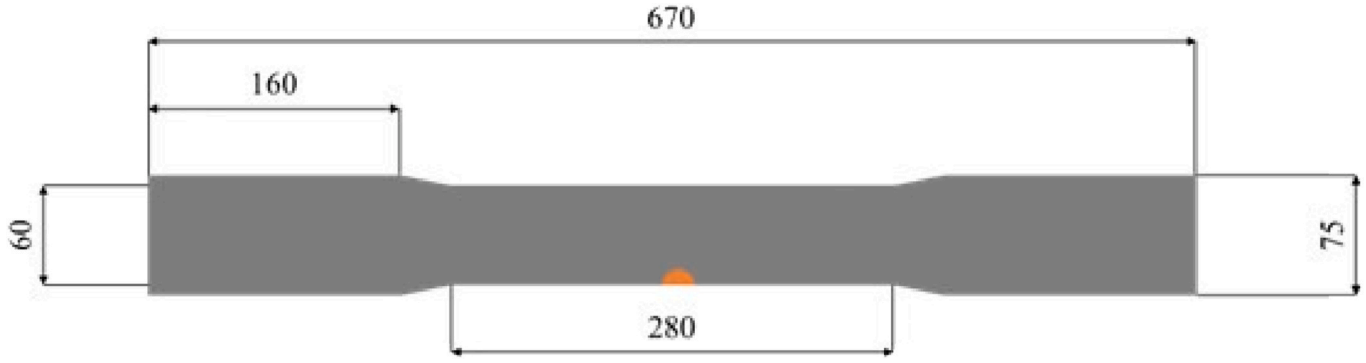

Fig. 6. Schematic representation of the dog-bone steel specimen (dimensions in mm). The thickness of the specimen is 8 mm.

the counter and the working electrode. Fig. 7 shows a schematic diagram of the three-electrode system.

Uniaxial fatigue loading was applied using an Instron axial-torsion servo-hydraulic testing machine (Fig. 4). The specimen was subjected to a sinusoidal cyclic loading regime with a maximum peak load of 168 kN, a load ratio of 0.18, and a loading frequency of 2 Hz. The tested coupon was subjected to an accelerated corrosion process for 100 h before the start of the accelerated corrosion-fatigue test. This process aims to simulate the initiation of surface defects and is referred to as 'pre-corrosion'. After the pre-corrosion process, accelerated corrosion (i.e. no cyclic load applied to the specimen) was alternated with accelerated corrosion-fatigue. A total of approximately 140 h of accelerated corrosion was reached by the end of the experiment. A total of approximately 270000 load cycles was performed during the corrosion-fatigue test. Fig. 8 shows a schematic of the testing conditions.

In order to estimate the contribution of fatigue and corrosion in the AE measurements, two situations are investigated: (i) corrosion-fatigue and (ii) corrosion-only. The difference between the two situations is

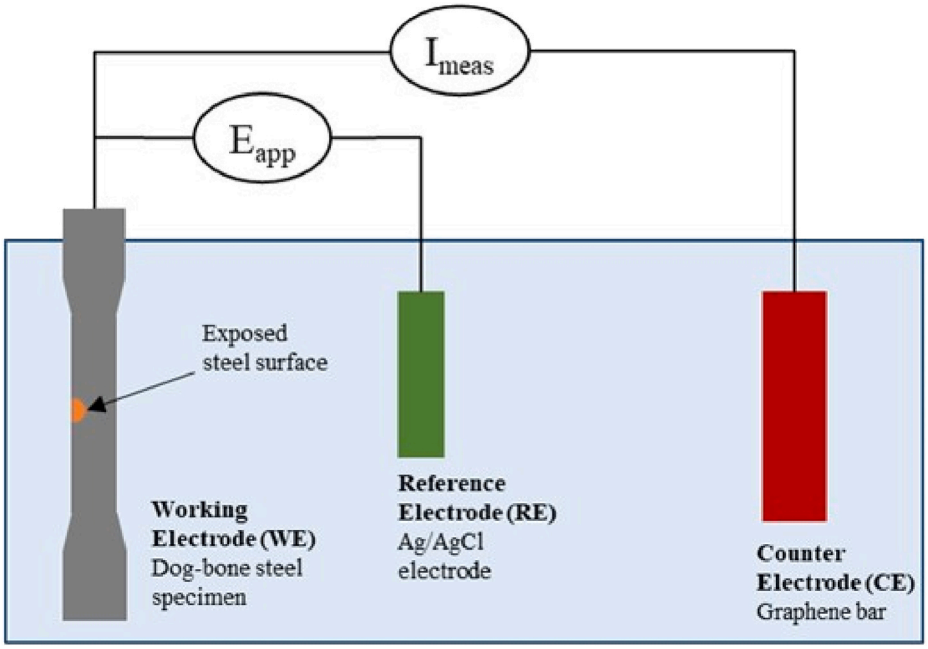

Fig. 7. Schematic illustration of the three-electrode system.

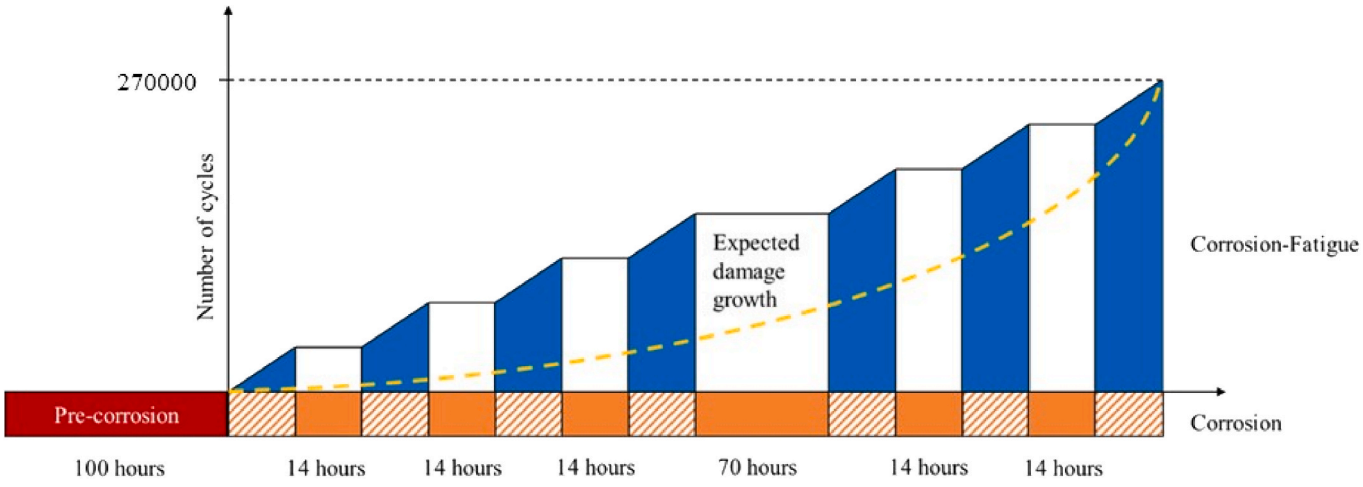

Fig. 8. Diagram of the testing conditions. Pre-corrosion process is indicated by the red solid fill. Accelerated corrosion (orange solid fill) is alternated with accelerated corrosion-fatigue (blue solid fill and orange diagonal stripes).

believed to provide insights into the contribution of fatigue.

3.3. Data acquisition, management, and quality control

To collect and record the ultrasound signals generated during the corrosion-fatigue process, an AMSY-6 Vallen data acquisition (DAQ) system and five watertight piezoelectric AE transducers (VS150-WIC-V01, with integrated preamplifier having a gain of 34 dB) were used. Piezoelectric AE sensors were connected to the DAQs using watertight coaxial cables. Fig. 9 shows a schematic of the sensor layout during the corrosion-fatigue test. The sensors were placed at a fixed distance from the specimen (7 cm) and held in position by a sensor holder (400 × 400mm^2 acrylic plate with a 7 x 7 grid of holes 5 cm equispaced). The fixed distance between the sensor holder and the specimen was measured with a laser meter (and confirmed with a tape measure) before testing. In practice keeping this distance constant during the measurement is preferable. However, as long as the relative position of the sensors in the measurement array is kept constant, the movement of the measurement array with respect to the specimen only shifts the calculated location of the damage (i.e. timing accuracy and damage activity indices remain unaffected), which can be further corrected by logging this relative position. The sensors were resonant piezoelectric AE transducers with a resonant frequency of 150 kHz and an operating frequency range of 50–450 kHz. The transfer function of the piezoelectric AE transducers can be found in Alkhateeb et al. (2022). In the proposed experimental setup, seawater is a couplant of ultrasound waves in contactless AE measurements. Removing seawater would require the placement of AE sensors on the surface of the specimen and the use of a different coupling medium (e.g. glue), which would change the measurement conditions.

With the expected AE signals in the range of a few hundred kHz and the transfer function of the selected transducers, a conservative sampling rate of 2.5 MHz for recording the ultrasound signal waveforms was selected, to ensure that no possible aliasing would occur. AE parameters, such as the peak amplitude, count, and energy, were extracted from the AE signals to monitor the evolution of the corrosion-fatigue damage.

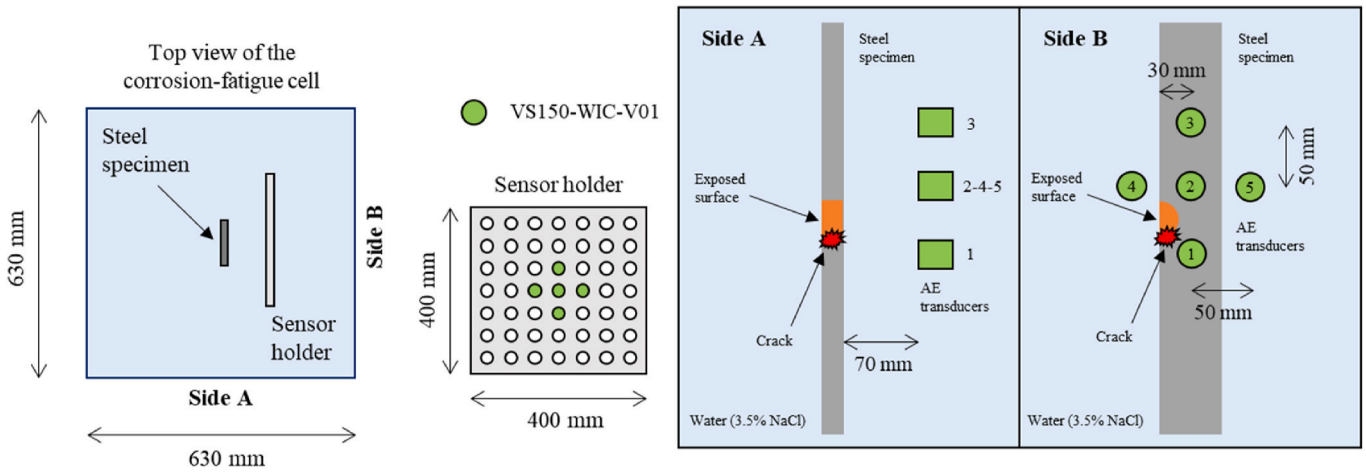

Fig. 9. Schematic illustration of the AE sensor layout.

The proper operation of the AE measurement system was verified before the corrosion-fatigue test by performing pencil lead break (PLB) tests according to ASTM E976-15 standards (ASTM E976-15, 2015) at different locations on the specimen (e.g. in the area of the exposed surface and outside). The noise level was assessed during the commissioning of the experimental setup. A dummy dog-bone steel specimen submerged in artificial seawater was subjected to cyclic loading (the same conditions as in the reported experiment) for 1 h. The measured noise level is approximately 50 dB.

The recorded ultrasound signals were pre-processed using a signal-to-noise ratio (SNR) filter of 6 dB to separate potential damage signals from background noise (i.e. continuous-type signals). In real-world offshore applications, underwater noise may be expected due to currents, ship propellers, waves, external operations, etc. Nonetheless, these sources are generally characterised by AE signatures with frequencies predominantly below 100 kHz (Cruz et al., 2021; Huang et al., 2023; Jiménez-Arranz et al., 2020), whereas corrosion-fatigue-induced AE signals are mostly pronounced in the range of 100–400 kHz.

4. Results and discussion

The experiments described in Section 3 were performed, and the methodology for the analysis of the ultrasound signals described in Section 2 was applied. The specimen was subjected to 100 h of pre-corrosion prior to corrosion-fatigue testing. During the corrosion-fatigue process, the specimen was subjected to approximately 270000 load cycles until failure. Approximately 140 h of corrosion were reached by the end of the experiment.

Fig. 10 shows the variation in the analysed AE parameters (i.e. peak amplitude, energy, and counts) as a function of the normalized number of load cycles (for all five sensors). Four stages of damage growth were identified (A-D, indicated by vertical black dashed lines), as previously suggested by Chai et al. (2018, 2022a), Han et al. (2011), Li et al. (2015), and Yu et al. (2011). Following the prior literature about the detection of different stages of damage growth using AE, the four stages can be referred to as macrocrack initiation (Stage A), growth of macrocrack with different crack growth rates (Stages B and C), and unstable crack growth and fracture (Stage D). The analysis of the measured peak amplitudes from different sensors during the corrosion-fatigue process provides valuable insights into the detectability of corrosion-fatigue damage using non-contact AE. Sensors 1, 2, and 4, which were the closest to the crack location, displayed similar acoustic activity throughout the corrosion-fatigue test. During Stage A, the peak amplitude ranges from 65 dB to 70 dB, indicating significant AE activity as the crack initiated and propagated. In Stage B, the amplitude decreases to 55–60 dB. At this stage, sensors 1 and 2 exhibited occasional jumps up to 65 dB, suggesting localised bursts of acoustic activity. This phenomenon is expected to have no adverse effect on the damage detection process. In fact, given the high SNR of these signals, they could serve as early indications of damage (after AE source localisation). Throughout Stage C, the peak amplitudes range from 55 dB to 75 dB. In Stage D, the amplitude ranges from 55 dB to 60 dB. Peak amplitudes up to 80 dB were recorded at the final failure of the specimen. Sensor 3 exhibited less variation in the peak amplitude throughout the test duration. The measured activity fluctuated within a range of 50–60 dB. During Stage D, which was close to the final failure stage, a distinct increase in peak amplitude was recorded. This trend was also evident in the activity measured using sensor 2. The increase in acoustic activity measured by sensors 2 and 3 during the critical stage (i.e. stage D) seems to detect the approaching failure. Sensor 5, located furthest from the crack location, recorded the lowest AE activity among all sensors. Despite the lower activity (compared to the other sensors), the measured peak amplitude still seems to follow the overall variations exhibited by sensors 1, 2, and 4. In the considered frequency range, geometric spreading is the leading factor influencing signal amplitude attenuation. Considering the background noise floor (i.e. 50 dB), the measurement results can be expected to hold up to 1 m from the specimen.

The analysis of the energy levels recorded by different sensors highlights the relevant trends in energy variations throughout the corrosion-fatigue test. Sensor 1 exhibited the highest energy levels among all sensors. Throughout the test, substantial variations in energy were recorded. During Stage A, bursts up to $1.5x10^4$ are observed, suggesting intense AE activity during damage initiation and propagation. In Stage B, the energy level remains below $0.5x10^4$, except for two instances already captured by the peak amplitude analysis. The activity of sensor 2 was similar to that of sensor 1. However, an observation was made during Stage D, close to the specimen failure. Sensor 2 showed increasing energy levels, possibly indicating AE activity leading to the impending failure of the specimen. Although sensor 3 recorded activity relatively similar to that of the other sensors, notable differences were observed. Sensor 3 captures 4–5 highly energetic bursts that were not highlighted by the behaviour of the peak amplitude. Additionally, sensor 3 showed a clear increasing trend in energy during Stage D, similar to sensor 2, indicating the potential importance of AE energy analysis in detecting approaching failure. Sensors 4 and 5 exhibit similar variations in AE energy. Sensor 5, which was furthest from the damage location, displayed the lowest energy levels (consistent with the measured peak amplitude). Despite the lower energy levels, the variations in energy captured by this sensor resembled those observed by other transducers, indicating its sensitivity in detecting AE activity. Although sensor placement seems to influence the measured energy levels, with sensors closer to the crack location generally detecting

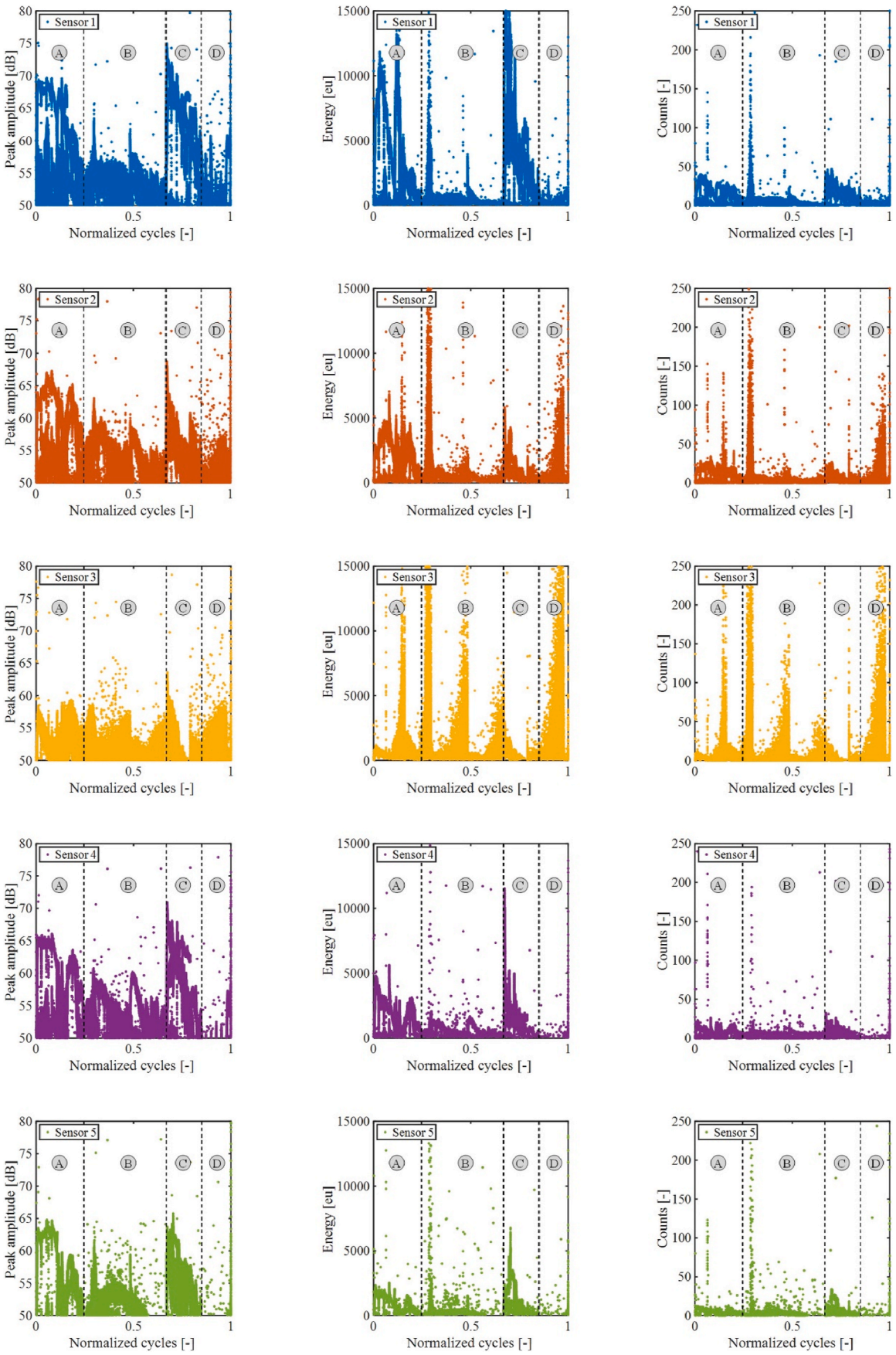

Fig. 10. Variation of AE parameters as a function of the normalized number of load cycles. Peak amplitude, energy, and counts are shown from left to right for every sensor.

higher energy levels, the analysis of AE energy highlights the importance of this parameter in detecting active sources of AE signals, especially during the critical stages leading to specimen failure.

The analysis of AE counts for damage detection during the corrosion-fatigue test presents both challenges and promising indications. In general, the AE counts exhibited less pronounced (compared to peak amplitude and energy) variations, remaining below 100 counts. Therefore, it is challenging to detect and identify active damage-induced sources. During the initial stages (A and B) of the test, all the sensors (1–5) record a few bursts of AE activity. Sensors 2 and 3 displayed the most remarkable behaviour in terms of AE counts. Sensor 2 exhibited a notably increasing trend in counts as the specimen failed. This trend is consistent with the observations from the energy and peak amplitude analyses, suggesting the potential of the AE counts to predict imminent failure. The same consideration can be made regarding the activity measured by sensor 3 during Stage D. The limited count variations and low values pose difficulties in identifying the active damage sources. However, sensors 2 and 3 exhibited promising behaviour close to specimen failure. When combined with other AE parameters such as energy and peak amplitude, AE counts can contribute significantly to the detection of damage.

Fig. 11 shows the variation and evolution of the rates of and cumulative AE parameters (i.e. burst-type signals, energy, and counts) as function of the normalized number of cycles (for all five sensors). The four stages of damage growth are labelled from A to D and distinguished by vertical black dashed lines.

Analysis of the AE hit rate obtained from different sensors during the corrosion-fatigue test provided valuable insights into the various stages of damage growth. Sensors 1, 2, and 4 exhibit similar AE hit rates throughout the test. In Stage A, the hit rate ranged from two to four hits per cycle, indicating high acoustic activity during the initiation of crack formation and propagation. Stage B shows a stable hit rate between 1 and 2 hits per cycle, indicating stable damage growth at a low rate. In Stage C, which is characterised by a higher rate of damage growth, the hit rate stabilises at three hits per cycle. In Stage D, differences emerged between the activities of the sensors. Remarkably, the behaviour of sensor 2, which exhibited an increasing trend in the hit rate from 0 to 4 hits per cycle before failure, suggests the occurrence of the specimen failure. Sensor 3 showed more variance in the hit rate measurements, making it challenging to distinguish between stages of damage growth. However, as with sensor 2, it shows a similar increasing AE hit rate (from 0 to 4.5 hits per cycle) when approaching final failure in Stage D. Sensor 5, which is the furthest from the damage location, recorded the lowest level of acoustic activity. Nonetheless, it still resembled the trend of AE activity with the most active sensors.

The cumulative number of AE signals provides clear distinctions between the different stages of damage growth. The slope of the cumulative signals is related to the AE hit rate and indicates how rapidly the damage grows. In Stage A, the slopes of the cumulative signals were relatively high during the initiation of crack formation and propagation. It decreased during Stage B because of the low rate of damage growth. In Stage C, the slope of the cumulative number of signals increases, possibly indicating a higher rate of damage growth. Stage D is characterised by a very low initial slope that increases close to failure, as observed in sensors 2 and 3. Fluctuations in the AE hit rate caused by bursts of acoustic activity were smoothened in the cumulative number of AE signals, providing a more stable representation of damage progression.

The analysis of the energy rates and cumulative energy levels during the corrosion-fatigue test also provided valuable indications of the stages of damage growth. Sensor 1 was the most active in terms of energy rate, followed by sensors 2, 4, and 3. Despite the varying energy rates among the sensors, an important consistent trend was observed. Stage A and C exhibited energy rate levels that were one order of magnitude higher than those in stages B and D. This indicates highly energetic activities during crack initiation and formation in Stage A and rapid damage growth in Stage C. Sensors 2 and 3 show a similar pattern, displaying an increasing trend in energy rate during Stage D. This signifies an escalation not only in the number of AE hits but also in the level of energy associated with each hit as it approaches final failure.

The cumulative energy also seems to add relevant information to the cumulative number of AE signals for identifying the damage growth stages. This is evident from the larger changes in the curve slopes. Stage B, characterised by low slope values, can be clearly distinguished from Stage A and C, which display steeper slopes, representing higher energy accumulation during these stages. Stage D shows a unique pattern of cumulative energy. It starts with an almost zero slope; however, as observed in sensor 3, the slope increases drastically close to failure.

An analysis of the AE count rate obtained from various sensors during the corrosion-fatigue test is also reported. Throughout the test, the count rate remained consistently below 100 counts/cycle. Although the count rates show limited variation, stage C exhibits the highest count rate, followed by stages A, B, and D. As shown in Fig. 10, the count rates obtained from sensors 2 and 3 increased steadily in Stage D. This consistent trend points towards the approaching critical failure stage.

The cumulative number of counts, whose trends resemble the cumulative energy, appears to be more effective (than the count rate) in distinguishing between different stages of damage growth.

The CVs of the peak amplitudes, energies, and counts are calculated and compared to quantify the performance of the parameters considered for the detection and identification of damage. The coefficient of variance is a measure of the dispersion of data around the mean and can be calculated by dividing the standard deviation by the mean of the data series. AE parameters with high CV values are typically preferred for damage detection and identification because they are associated with larger data dispersion. Large data dispersion indicates the presence of different AE source mechanisms (Chai et al., 2017). Table 1 lists the calculated CV values of selected AE parameters. For all considered sensors, the AE energy exhibited the highest CV value. This suggests that AE energy is the most effective parameter (among the selected parameters) for the detection and identification of damage evolution in the steel specimen. The higher value of CV displayed by sensor 5 is caused by the lower mean of the AE energy characterising its measurements.

The mean energy of the AE signals was calculated for each stage of damage growth. Fig. 12 compares the mean energies of the corrosion- and corrosion-fatigue-induced signals throughout the different stages of damage growth. Decoupling of the corrosion- and corrosion-fatigue-induced signals was done based on the testing conditions and on the assumption that during corrosion-fatigue the degradation of the material was mainly caused by the fatigue process. Analysis of the mean energy at different stages of the test provided valuable insights into the energy characteristics of corrosion- and corrosion-fatigue-induced signals during damage evolution. The mean energy of the corrosion-induced signals appeared to be relatively stable and was limited to values below 500 eu. The mean energy of the corrosion-induced signals was approximately one order of magnitude lower than that of the corrosion-fatigue-induced signals. Regarding the corrosion-fatigue-induced signals, in the initial Stage A, mean energy displays relatively high values. As the damage progressed to Stage B, the mean energy decreased. During Stages C and D, the mean energy experienced a drastic increase, reaching magnitudes on the order of 10^5 at the end of the test (because of the final failure of the specimen). Despite the complexity of the corrosion-induced damage mechanisms, based on this result, the corrosion process seems to induce less energy (confirming the considerations in Section 2.1) and more stable acoustic activity (possibly indicating a more controlled degradation process). In contrast, the corrosion-fatigue-induced damage exhibited a more intense and dynamic energy distribution, suggesting a more severe and less consistent material degradation mechanism. Finally, the rapid and substantial increase in the corrosion-fatigue-induced mean energy may be an indication of accelerated material degradation as it approaches the final failure.

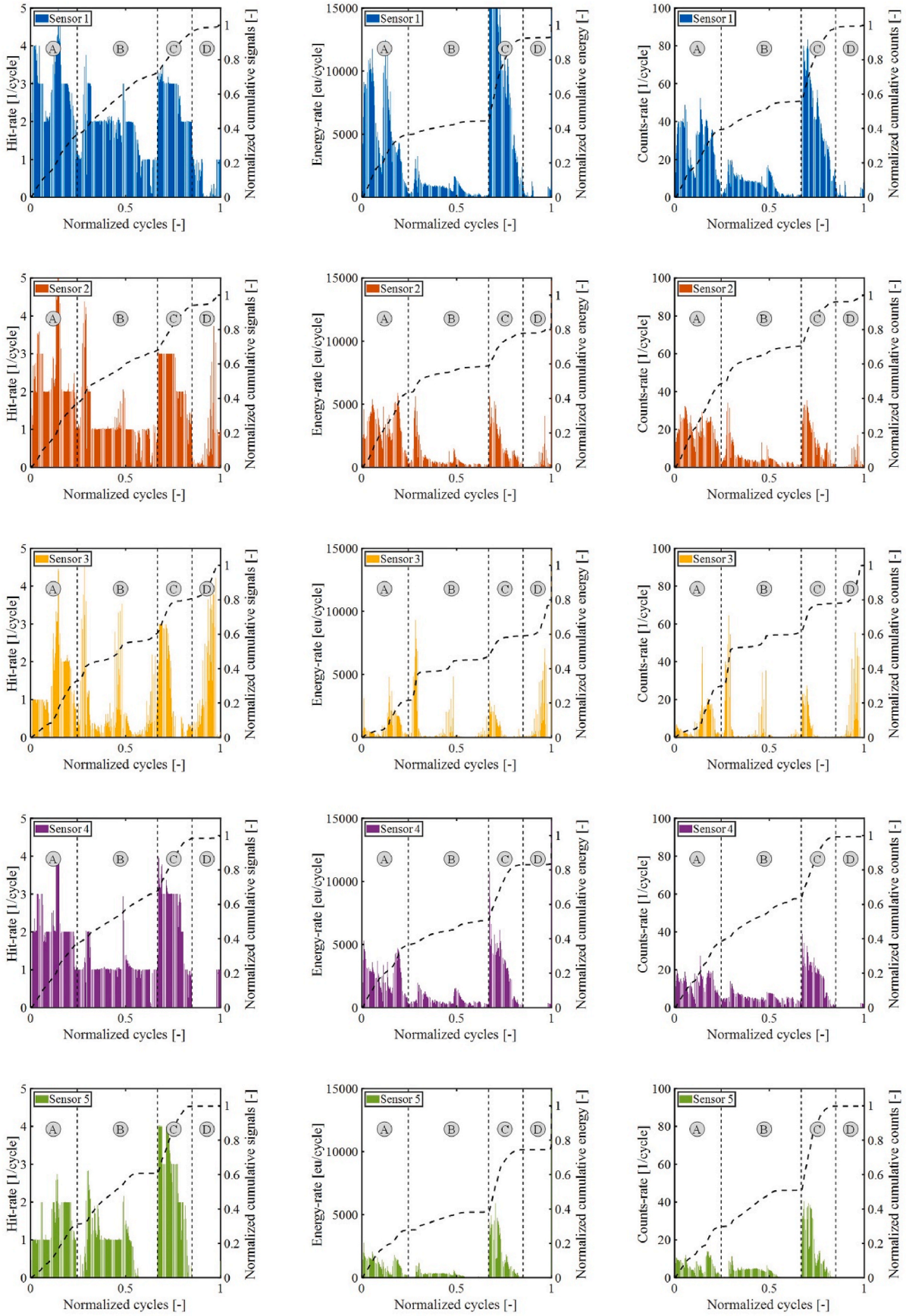

Fig. 11. Variation and evolution of rate and cumulative AE parameters as a function of the normalized number of load cycles. Hits, energy, and counts are shown from left to right for every sensor.

Table 1
Coefficient of Variance (CV) of the selected AE time domain parameters.

AE parameter	Amplitude	Energy	Counts
Sensor 1	0.99	2.09	1.30
Sensor 2	1.09	2.99	1.85
Sensor 3	1.67	3.74	3.29
Sensor 4	1.01	2.24	1.74
Sensor 5	1.11	4.26	1.99

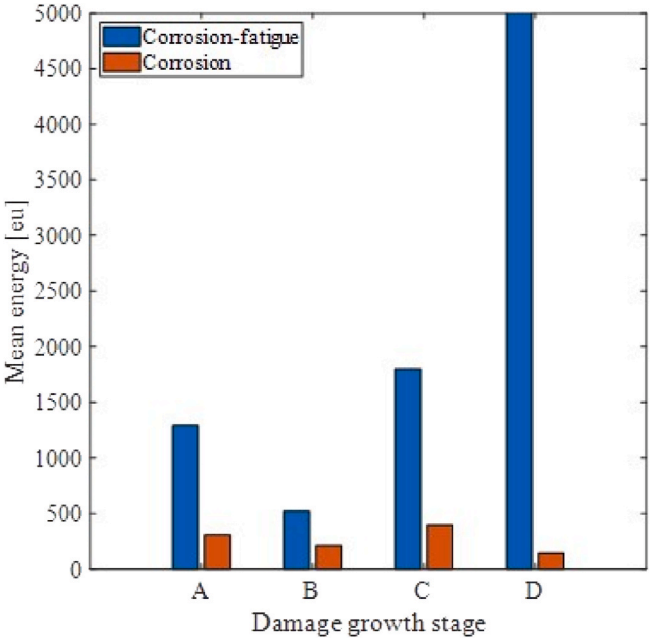

Fig. 12. Mean energy of corrosion- and corrosion-fatigue-induced signals during different stages of damage growth.

The relative contributions of the corrosion- and corrosion-fatigue-induced ultrasound signals throughout the experiment are defined as the number of burst-type signals per hour of testing. Fig. 13 shows the relative contributions in the four different stages of damage growth.

The total numbers of corrosion- and corrosion-fatigue-induced ultrasound signals at different stages of damage growth are shown in Fig. 14.

Combined with the insights in Fig. 13, it can be inferred that the contribution of the corrosion-induced signals did not exceed 2% of the total number of measured signals (per hour of testing). During stages A and C, the corrosion-induced signals were limited to 1% of the total

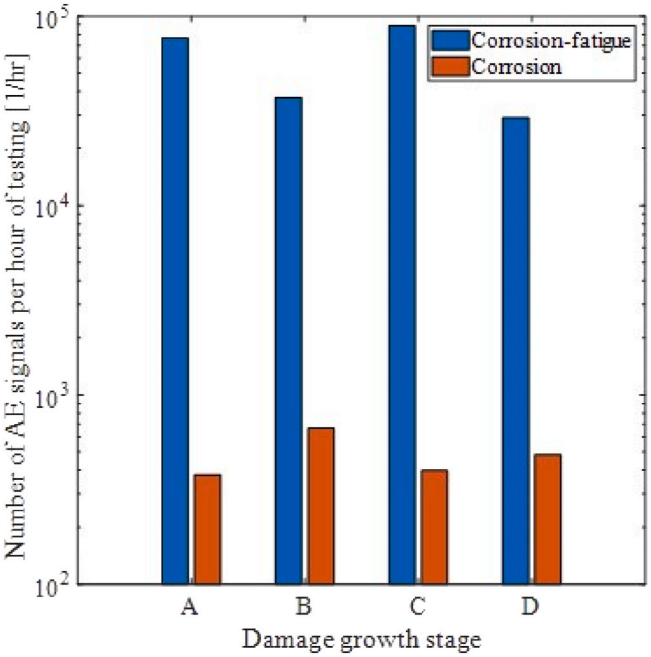

Fig. 14. Total number of corrosion- and corrosion-fatigue-induced signals per hour of testing during different stages of damage growth.

number of signals. In stages A and C, 378 and 397 corrosion-induced signals were detected, respectively, while 76717 and 88745 corrosion-fatigue-induced AE signals were observed. Stages B and D showed the highest relative contribution of corrosion-induced signals, at 2% of the total measured signals. A total of 666 and 483 corrosion-induced signals were measured, against 37132 and 29073 corrosion-fatigue-induced AE signals during stages B and D, respectively. Although in the proposed experimental set-up, the corrosion mechanism seems to induce a lower number of ultrasound signals (at a lower energy level) than the corrosion-fatigue mechanism, it can be concluded that corrosion-induced signals can be detected throughout the evolution of the corrosion-fatigue damage.

The condition of the exposed surface during the test is shown in Fig. 15. At the start of the test, after the pre-corrosion process, the exposed surface shows uniform corrosion and a thin oxide layer. In Stage A, corrosion appears more uniform, and bubbles form on the specimen's surface. In Stage B, fewer bubbles are visible, and the surface continues to show uniform corrosion. A thicker oxide layer forms and the water becomes turbid due to the release of iron ions into the solution. In Stage C, bubbles appear on the edges of the specimen along with corrosion

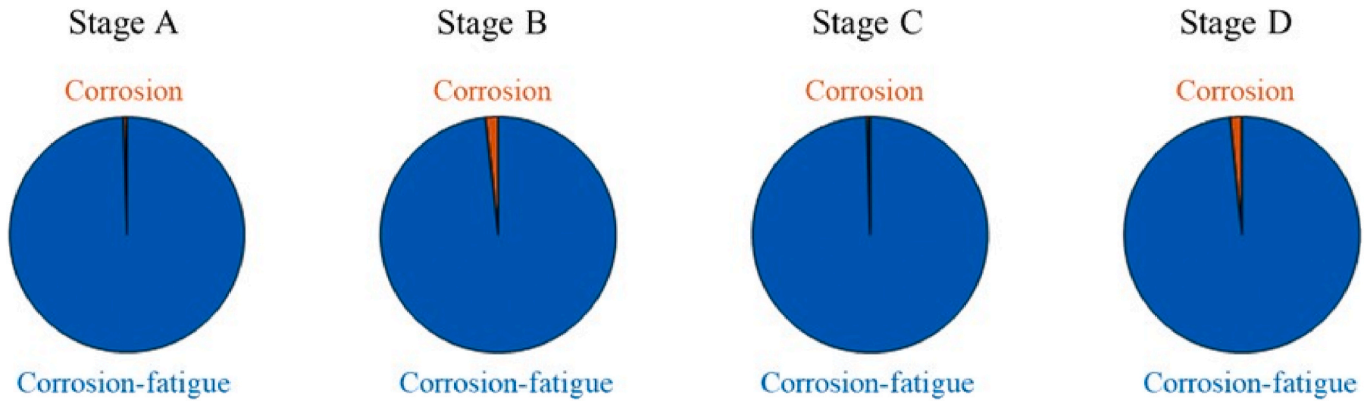

Fig. 13. Average number of corrosion- and corrosion-fatigue-induced signals per hour of testing during different stages of damage growth. Stages A to D are shown from left to right.

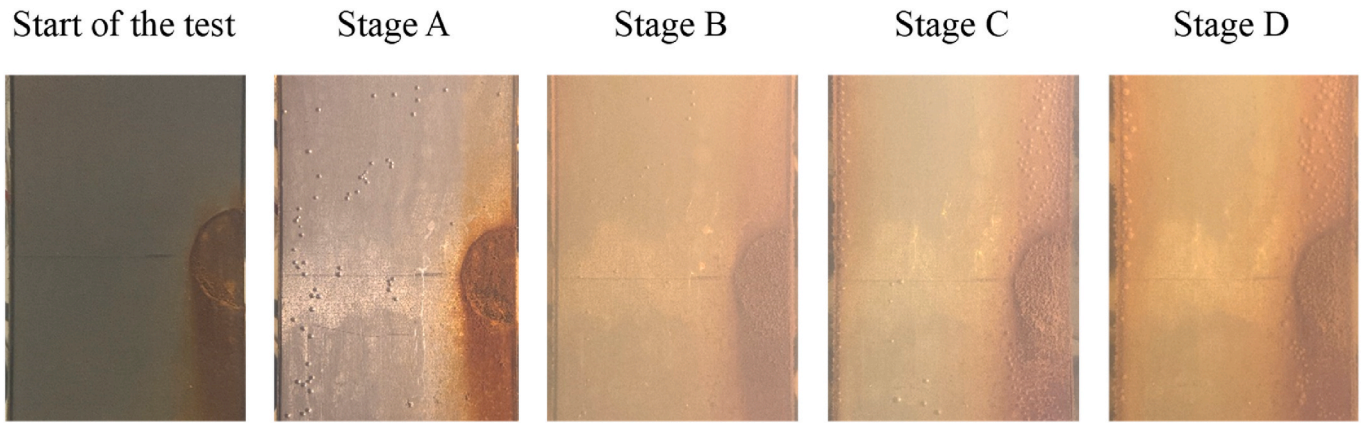

Fig. 15. Exposed surface condition during different stages of the experiment.

activity. This likely occurred after part of the coating layer detached from the specimen surface. The exposed surface shows a thicker oxide layer. In stage D, fewer but larger bubbles are present. The oxide layer is thicker and more uniform, and water turbidity increases. Both the mean energy (Fig. 12) and the number of signals (Fig. 14) exhibit limited fluctuations in corrosion-induced acoustic activity, suggesting a stable degradation process. This is further supported by the consistent growth of the oxide layer on the exposed surface. Additionally, the continuous increase in water turbidity suggests an ongoing corrosion process. The appearance of bubbles and the coating layer detachment may influence the corrosion dynamics. These factors can be expected to be sources of the fluctuations in the corrosion-induced AE activity.

5. Conclusions

Corrosion-fatigue experiments were conducted on a dog-bone steel specimen to assess the detectability of corrosion-fatigue damage using non-contact AE. Corrosion-fatigue was successfully induced using the proposed experimental setup, and damage-induced ultrasound signals were detected with a satisfactory signal-to-noise ratio using non-contact AE sensors (in the frequency range of 50–450 kHz).

The trends in the AE parameters over the load cycles revealed four stages of damage evolution (from A to D). The cumulative number of AE signals shows clear distinctions between the stages, smoothing fluctuations in the rates and providing a more stable representation of damage progression. The energy rate trends suggest highly energetic activity during crack formation and rapid growth in stages A and C, respectively.

Among the considered parameters, the AE energy exhibited the highest variability, making it an effective indicator of the damage evolution in the specimen. A comparison of mean energy levels throughout the experiment differentiated corrosion- and corrosion-fatigue-induced signals, with the latter exhibiting a mean energy approximately one order of magnitude higher than that of the former. In the proposed experiment, it appeared that the corrosion mechanism induced a significantly lower number of ultrasound signals than corrosion-fatigue; however, it was possible to detect corrosion-induced signals throughout the entire damage evolution.

Although the results offer high potential for the identification and monitoring of corrosion-fatigue damage using non-contact AE, further experiments under different mechanical and electrochemical conditions are needed to extend the conclusions of this study. Further data processing, for example, AE source localisation, will also be required to distinguish different AE source mechanisms and quantitatively assess their evolution during the corrosion-fatigue process.

CRediT authorship contribution statement

Filippo Riccioli: Writing – original draft, Visualization, Software, Methodology, Investigation, Formal analysis, Data curation, Conceptualization. **Sarjoon Alkhateeb:** Writing – review & editing. **Arjan Mol:** Writing – review & editing. **Lotfollah Pahlavan:** Writing – review & editing, Supervision, Resources, Project administration, Methodology, Funding acquisition, Conceptualization.

Declaration of competing interest

The authors declare that they have no known competing financial interests or personal relationships that could have appeared to influence the work reported in this paper.

Acknowledgements

This research has been conducted within the framework of Donut Joint Industry Project (JIP). The project partners are acknowledged for their support and contribution. Donut JIP has been made possible by the financial contribution of TKI Maritime.

References

Adedipe, O., Brennan, F., Kolios, A., 2016. Review of corrosion fatigue in offshore structures: present status and challenges in the offshore wind sector. Renew. Sustain. Energy Rev. 61, 141–154. https://doi.org/10.1016/j.rser.2016.02.017.

Aggelis, D.G., Kordatos, E.Z., Matikas, T.E., 2011. Acoustic emission for fatigue damage characterization in metal plates. Mech. Res. Commun. 38 (2), 106–110. https://doi.org/10.1016/j.mechrescom.2011.01.011.

Alkhateeb, S., Riccioli, F., Morales, F.L., Pahlavan, L., 2022. Non-contact acoustic emission monitoring of corrosion under marine growth. Sensors 23 (1), 161. https://doi.org/10.3390/s23010161.

Arzaghi, E., Abbassi, R., Garaniya, V., Binns, J., Chin, C., Khakzad, N., Reniers, G., 2018. Developing a dynamic model for pitting and corrosion-fatigue damage of subsea pipelines. Ocean Eng. 150, 391–396. https://doi.org/10.1016/j.oceaneng.2017.12.014.

Assaker, J.P., 2020. Underwater inspection of fixed offshore steel structures. Available online: https://iumi.com/news/iumieye-newsletter-september-2020/underwater-inspection-of-fixed-offshore-steel-structures. (Accessed 3 April 2023).

ASTM E8/E8M-22, 2022. Standard test methods for tension testing of metallic materials. American Society of Testing of Materials: West Conshohocken, PA, USA.

ASTM E976-15, 2015. Standard guide for determining the reproducibility of acoustic emission sensor response. American Society of Testing of Materials. West Conshohocken, PA, USA.

Bhandari, J., Khan, F., Abbassi, R., Garaniya, V., Ojeda, R., 2015. Modelling of pitting corrosion in marine and offshore steel structures–A technical review. J. Loss Prev. Process. Ind. 37, 39–62. https://doi.org/10.1016/j.jlp.2015.06.008.

Bi, H., Li, H., Zhang, W., Wang, L., Zhang, Q., Cao, S., Toku-Gyamerah, I., 2020. Evaluation of the acoustic emission monitoring method for stress corrosion cracking on aboveground storage tank floor steel. Int. J. Pres. Ves. Pip. 179, 104035. https://doi.org/10.1016/j.ijpvp.2019.104035.

Caines, S., Khan, F., Shirokoff, J., 2013. Analysis of pitting corrosion on steel under insulation in marine environments. J. Loss Prev. Process. Ind. 26 (6), 1466–1483. https://doi.org/10.1016/j.jlp.2013.09.010.

Calabrese, L., Bonaccorsi, L., Galeano, M., Proverbio, E., Di Pietro, D., Cappuccini, F., 2015. Identification of damage evolution during SCC on 17-4 PH stainless steel by combining electrochemical noise and acoustic emission techniques. Corrosion Sci. 98, 573–584. https://doi.org/10.1016/j.corsci.2015.05.063.

Calabrese, L., Proverbio, E., 2020. A review on the applications of acoustic emission technique in the study of stress corrosion cracking. Corrosion and Materials Degradation 2 (1), 1–30. https://doi.org/10.3390/cmd2010001.
Chai, M., Zhang, J., Zhang, Z., Duan, Q., Cheng, G., 2017. Acoustic emission studies for characterization of fatigue crack growth in 316LN stainless steel and welds. Appl. Acoust. 126, 101–113. https://doi.org/10.1016/j.apacoust.2017.05.014.
Chai, M., Zhang, Z., Duan, Q., 2018. A new qualitative acoustic emission parameter based on Shannon's entropy for damage monitoring. Mech. Syst. Signal Process. 100, 617–629. https://doi.org/10.1016/j.ymssp.2017.08.007.
Chai, M., Lai, C., Xu, W., Duan, Q., Zhang, Z., Song, Y., 2022a. Characterization of fatigue crack growth based on acoustic emission multi-parameter analysis. Materials 15 (19), 6665. https://doi.org/10.3390/ma15196665.
Chai, M., Hou, X., Zhang, Z., Duan, Q., 2022b. Identification and prediction of fatigue crack growth under different stress ratios using acoustic emission data. Int. J. Fatig. 160, 106860. https://doi.org/10.1016/j.ijfatigue.2022.106860.
Chang, H., Han, E., Wang, J.Q., Ke, W., 2005. Acoustic emission study of corrosion fatigue crack propagation mechanism for LY12CZ and 7075-T6 aluminum alloys. J. Mater. Sci. 40, 5669–5674. https://doi.org/10.1007/s10853-005-1300-9.
Cruz, E., Lloyd, T., Bosschers, J., Lafeber, F.H., Vinagre, P., Vaz, G., 2021. Study on Inventory of Existing Policy, Research and Impacts of Continuous Underwater Noise in Europe. WavEC Offshore Renewables and Maritime Research Institute Netherlands. EMSA report EMSA/NEG/21/2020.
Du, G., Li, J., Wang, W.K., Jiang, C., Song, S.Z., 2011. Detection and characterization of stress-corrosion cracking on 304 stainless steel by electrochemical noise and acoustic emission techniques. Corrosion Sci. 53 (9), 2918–2926. https://doi.org/10.1016/j.corsci.2011.05.030.
Du, J., Wang, H., Wang, S., Song, X., Wang, J., Chang, A., 2020. Fatigue damage assessment of mooring lines under the effect of wave climate change and marine corrosion. Ocean Eng. 206, 107303. https://doi.org/10.1016/j.oceaneng.2020.107303.
Ferrer, F., Faure, T., Goudiakas, J., Andrès, E., 2002. Acoustic emission study of active–passive transitions during carbon steel erosion–corrosion in concentrated sulfuric acid. Corrosion Sci. 44 (7), 1529–1540. https://doi.org/10.1016/S0010-938X(01)00148-2.
Fontaine, E., Rosen, J., Potts, A., Ma, K.T., Melchers, R., 2014a. Scorch jip-feedback on MIC and pitting corrosion from field recovered mooring chain links. In: Offshore Technology Conference. OnePetro. https://doi.org/10.4043/25234-MS
Fontaine, E., Kilner, A., Carra, C., Washington, D., Ma, K.T., Phadke, A., Laskowski, D., Kusinski, G., 2014b. Industry survey of past failures, pre-emptive replacements and reported degradations for mooring systems of floating production units. In: Offshore Technology Conference. OnePetro. https://doi.org/10.4043/25273-MS.
Forsyth, D.S., 2011. Non-destructive testing for corrosion. Corrosion Fatigue and Environmentally Assisted Cracking in Aging Military Vehicles. RTO-AG-AVT-140).
Fregonese, M., Idrissi, H., Mazille, H., Renaud, L., Cetre, Y., 2001. Initiation and propagation steps in pitting corrosion of austenitic stainless steels: monitoring by acoustic emission. Corrosion Sci. 43 (4), 627–641. https://doi.org/10.1016/S0010-938X(00)00099-8.
Grosse, C., 2008. In: Grosse, C.U., Ohtsu, M. (Eds.), Acoustic Emission Testing. https://doi.org/10.1007/978-3-540-69972-9.
Han, Z., Luo, H., Cao, J., Wang, H., 2011. Acoustic emission during fatigue crack propagation in a micro-alloyed steel and welds. Mater. Sci. Eng. 528 (25–26), 7751–7756. https://doi.org/10.1016/j.msea.2011.06.065.
Huang, L.F., Xu, X.M., Yang, L.L., Huang, S.Q., Zhang, X.H., Zhou, Y.L., 2023. Underwater noise characteristics of offshore exploratory drilling and its impact on marine mammals. Front. Mar. Sci. 10, 1097701.
Huijer, A., Kassapoglou, C., Pahlavan, L., 2021. Acoustic emission monitoring of carbon fibre reinforced composites with embedded sensors for in-situ damage identification. Sensors 21 (20), 6926. https://doi.org/10.3390/s21206926.
Hwang, W., Bae, S., Kim, J., Kang, S., Kwag, N., Lee, B., 2015. Acoustic emission characteristics of stress corrosion cracks in a type 304 stainless steel tube. Nucl. Eng. Technol. 47 (4), 454–460. https://doi.org/10.1016/j.net.2015.04.001.
Jiménez-Arranz, G., Banda, N., Cook, S., Wyatt, R., 2020. Review of Existing Data on Underwater Sounds Produced by the Oil and Gas Industry. JIP Topic-Sound Source Characterisation and Propagation.
Jirarungsatian, C., Prateepasen, A., 2010. Pitting and uniform corrosion source recognition using acoustic emission parameters. Corrosion Sci. 52 (1), 187–197. https://doi.org/10.1016/j.corsci.2009.09.001.
Kim, J.K., Kee, S.H., Futalan, C.M., Yee, J.J., 2019. Corrosion monitoring of reinforced steel embedded in cement mortar under wet-and-dry cycles by electrochemical impedance spectroscopy. Sensors 20 (1), 199. https://doi.org/10.3390/s20010199.
Kinsler, L.E., Frey, A.R., Coppens, A.B., Sanders, J.V., 2000. Fundamentals of Acoustics. John wiley & sons.
Krautkrämer, J., Krautkrämer, H., 2013. Ultrasonic Testing of Materials. Springer Science & Business Media.
Li, L., Zhang, Z., Shen, G., 2015. Influence of grain size on fatigue crack propagation and acoustic emission features in commercial-purity zirconium. Mater. Sci. Eng. 636, 35–42. https://doi.org/10.1016/j.msea.2015.03.046.
Lone, E.N., Sauder, T., Larsen, K., Leira, B.J., 2022a. Probabilistic fatigue model for design and life extension of mooring chains, including mean load and corrosion effects. Ocean Eng. 245, 110396. https://doi.org/10.1016/j.oceaneng.2021.110396.
Lone, E.N., Sauder, T., Larsen, K., Leira, B.J., 2022b. Fatigue reliability of mooring chains, including mean load and corrosion effects. Ocean Eng. 266, 112621. https://doi.org/10.1016/j.oceaneng.2022.112621.
Ma, K.T., Shu, H., Smedley, P., L'Hostis, D., Duggal, A., 2013. A historical review on integrity issues of permanent mooring systems. In: Offshore Technology Conference. OnePetro. https://doi.org/10.4043/24025-MS.
Mansfeld, F., Little, B., 1991. A technical review of electrochemical techniques applied to microbiologically influenced corrosion. Corrosion Sci. 32 (3), 247–272. https://doi.org/10.1016/0010-938X(91)90072-W.
McCluney, S.A., Popova, S.N., Popov, B.N., White, R.E., Griffin, R.B., 1992. Comparing electrochemical impedance spectroscopy methods for estimating the degree of delamination of organic coatings on steel. J. Electrochem. Soc. 139 (6), 1556. https://doi.org/10.1149/1.2069454.
Melchers, R.E., Jeffrey, R., Fontaine, E., 2012. Corrosion and the structural safety of FPSO mooring systems in Tropical waters. In: Proceedings of the Australasian Structural Engineering Conference, pp. 11–13. Perth, WA, Australia.
Meyer, R.M., Pardini, A.F., Hanson, B.D., Sorenson, K.B., 2013. Review of NDE Methods for Detection and Monitoring of Atmospheric SCC in Welded Canisters for the Storage of Used Nuclear Fuel (No. PNNL-22158). Pacific Northwest National Lab. (PNNL), Richland, WA (United States).
Nuthalapati, S., Kee, K.E., Pedapati, S.R., Jumbri, K., 2023. A review of chloride induced stress corrosion cracking characterization in austenitic stainless steels using acoustic emission technique. Nucl. Eng. Technol. https://doi.org/10.1016/j.net.2023.11.005.
Pahlavan, P.L., Paulissen, J., Pijpers, R., Hakkesteegt, H., Jansen, R., 2014. Acoustic emission health monitoring of steel bridges. In: EWSHM-7th European Workshop on Structural Health Monitoring.
Qian, W., Wu, S., Lei, L., Hu, Q., Liu, C., 2024. Time lapse in situ X-ray imaging of failure in structural materials under cyclic loads and extreme environments. J. Mater. Sci. Technol. 175, 80–103. https://doi.org/10.1016/j.jmst.2023.07.041.
Ribeiro, D.V., Abrantes, J.C.C., 2016. Application of electrochemical impedance spectroscopy (EIS) to monitor the corrosion of reinforced concrete: a new approach. Construct. Build. Mater. 111, 98–104. https://doi.org/10.1016/j.conbuildmat.2016.02.047.
Rizzo, P., 2013. NDE/SHM of underwater structures: a review. Adv. Sci. Technol. 83, 208–216. https://doi.org/10.4028/www.scientific.net/AST.83.208.
Roberge, P.R., 2008. Corrosion Engineering: Principles and Practice. McGraw Hill, New York, NY, USA.
Scheeren, B., Kaminski, M.L., Pahlavan, L., 2022. Evaluation of ultrasonic stress wave transmission in cylindrical roller bearings for acoustic emission condition monitoring. Sensors 22 (4), 1500. https://doi.org/10.3390/s22041500.
Scheeren, B., Kaminski, M.L., Pahlavan, L., 2023. Acoustic emission monitoring of naturally developed damage in large-scale low-speed roller bearings. Struct. Health Monit. 23 (1), 360–382. https://doi.org/10.1177/14759217231164912.
Skal's' Kyi, V.R., Nazarchuk, Z.T., Dolins' ka, I.Y., Yarema, R.Y., Selivonchyk, T.V., 2017. Acoustic-emission diagnostics of corrosion defects in materials (a survey). Part. 1. Detection of electrochemical corrosion and corrosion fatigue. Mater. Sci. 53, 295–305. https://doi.org/10.1007/s11003-017-0075-x.
Stannard, T.J., Williams, J.J., Singh, S.S., Singaravelu, A.S.S., Xiao, X., Chawla, N., 2018. 3D time-resolved observations of corrosion and corrosion-fatigue crack initiation and growth in peak-aged Al 7075 using synchrotron X-ray tomography. Corrosion Sci. 138, 340–352. https://doi.org/10.1016/j.corsci.2018.04.029.
Van Steen, C., Pahlavan, L., Wevers, M., Verstrynge, E., 2019. Localisation and characterisation of corrosion damage in reinforced concrete by means of acoustic emission and X-ray computed tomography. Construct. Build. Mater. 197, 21–29. https://doi.org/10.1016/j.conbuildmat.2018.11.159.
Wang, R., Luo, S., Liu, M., Xue, Y., 2014. Electrochemical corrosion performance of Cr and Al alloy steels using a J55 carbon steel as base alloy. Corrosion Sci. 85, 270–279. https://doi.org/10.1016/j.corsci.2014.04.023.
Wang, Y.S., Liu, L., Fu, Q., Sun, J., An, Z.Y., Ding, R., Li, Y., Zhao, X.D., 2020. Effect of Bacillus subtilis on corrosion behavior of 10MnNiCrCu steel in marine environment. Sci. Rep. 10 (1), 5744. https://doi.org/10.1038/s41598-020-62809-y.
Yu, J., Ziehl, P., Zárate, B., Caicedo, J., 2011. Prediction of fatigue crack growth in steel bridge components using acoustic emission. J. Constr. Steel Res. 67 (8), 1254–1260. https://doi.org/10.1016/j.jcsr.2011.03.005.
Yuyama, S., Hisamatsu, Y., Kishi, T., 1984. Fundamental aspects of AE monitoring on corrosion fatigue processes in austenitic stainless steel. J. Mater. Energy Syst. 5 (4). https://doi.org/10.1007/BF02835719.
Zawawi, N.A., Liew, M.S., Alaloul, W.S., Shawn, L.E., Imran, M., Toloue, I., 2019. Non-Destructive testing techniques for offshore underwater decommissioning projects through cutting detection: a state of review. In: SPE Symposium: Decommissioning and Abandonment. OnePetro. https://doi.org/10.2118/199191-MS
Zhang, X., Hoogeland, M., 2019. Influence of deformation on corrosion of mooring chain steel in seawater. Mater. Corros. 70 (6), 962–972. https://doi.org/10.1002/maco.201810766.
Zhang, X., Noël-Hermes, N., Ferrari, G., Hoogeland, M., 2022. Localized corrosion of mooring chain steel in seawater. Corrosion and Materials Degradation 3 (1), 53–74. https://doi.org/10.3390/cmd3010004.